Statistical Relationships between Two Types of Heavy Rainfall and Low-Level Jets in South China

XIAOQING LI[a,b,c] AND YU DU[a,b,c]

[a] *School of Atmospheric Sciences, Sun Yat-sen University, Southern Marine Science and Engineering Guangdong Laboratory (Zhuhai), Zhuhai, China*
[b] *Guangdong Province Key Laboratory for Climate Change and Natural Disaster Studies, Sun Yat-sen University, China*
[c] *Key Laboratory of Tropical Atmosphere-Ocean System (Sun Yat-sen University), Ministry of Education, China*

(Manuscript received 7 February 2021, in final form 28 July 2021)

ABSTRACT: Two types of heavy rainfall, namely warm-sector and frontal heavy rainfall, coexist in South China during the presummer rainy season and manifest as varying mechanisms and features. They both exhibit close relationships with two types of low-level jets (LLJs): the boundary layer jet (BLJ) and synoptic-system-related low-level jet (SLLJ), but in different ways. The motivation of the present study is to elucidate the statistical relations between the two types of heavy rainfall and LLJs over South China using TRMM rainfall data and ERA5 reanalysis. Generally, warm-sector heavy rainfall mainly occurs over coastal areas and during the early morning, which is primarily caused by the interaction between the nocturnal BLJ and land breeze. In contrast, frontal heavy rainfall is mostly concentrated in inland regions and modulated by distinct diurnal forcings at different locations. Statistical analysis indicates that 76% (62%) of the warm-sector (frontal) heavy rainfall events are associated with LLJs. In the presence of heavy rainfall, low-level winds are often strengthened over Beibu Gulf, northern South China Sea, and the south side of fronts, corresponding to two branches of southerly BLJs at ~950 hPa over the ocean and the southwesterly SLLJs at ~850–700 hPa on land, respectively. Furthermore, BLJs are shown to be linked to both types of heavy rainfall and with the most frequent occurrences of rainfall in their exit region, whereas SLLJs are more closely associated with frontal heavy rainfall. The left side (entrance) of the SLLJ axis is favorable for frontal (warm-sector) heavy rainfall production. The regional rainfall distributions are affected by the structures and locations of LLJs.

KEYWORDS: Mesoscale processes; Jets; Rainfall

1. Introduction

Frequent occurrences of heavy rainfall rank as the primary weather-related disasters in South China during the presummer rainy season (April–June; Luo et al. 2017). Heavy rainfall in this rainy season, which contributes about 50% of the annual rainfall, is often generated by mesoscale convective systems (MCSs; Luo et al. 2017; Sun et al. 2019). The environmental condition of the heavy rainfall is often characterized by southwesterly monsoon or significant synoptic disturbances (e.g., cold or quasi-stationary fronts; Li et al. 2020). Considering whether it is driven by weak or strong synoptic-scale forcing, the heavy rainfall can be classified into two types: warm-sector heavy rainfall (WR hereafter) and frontal heavy rainfall (FR hereafter; e.g., Huang 1986; Ding 1994). Climatological comparison by Wu et al. (2020) showed that WR favors coastal regions of Guangdong Province and within the warm sector that is located a few hundred kilometers ahead of a cold front or in the absence of a cold front, while FR often occurs over the inland areas in northern Guangdong and is associated with the passage of fronts. Compared to FR, WR is found to be characterized by strong intensity, concentrated precipitation, and sudden occurrences, and thus has low predictability (Huang 1986; Ding 1994; Luo et al. 2017; Huang and Luo 2017; Du and Chen 2018; Wu et al. 2020).

Previous studies have emphasized the important role of LLJs in heavy rainfall. The presence of LLJs is recognized as a key factor for convection initiation, organization, maintenance, and propagation through enhanced moisture supply and energy transportation to the rainfall regions (Higgins et al. 1997; Liu et al. 2014; Luo et al. 2017; Du and Chen 2019b). LLJs can affect the diurnal variation of rainfall through their diurnal cycles in wind speed and direction (Du and Chen 2019b; Wu et al. 2020; Du et al. 2020a). Moreover, LLJs can induce low-level convergence and upward motion in their exit region (Tao and Chen 1987; G. Chen et al. 2017; Hodges and Pu 2018; Du and Chen 2019a). In addition to the exit region, some previous studies have documented another preferred location for heavy rainfall—along the left side of the LLJ axis—due to positive vorticity (Beebe and Bates 1955; Walters and Winkler 2001) and mass convergence (Xia et al. 2006; Xia and Zhao 2009; Zhang and Ni 2009). The left-front sector of LLJs with great inertial stability is also found to be efficient in the accumulation of warm moist air (Zhang and Zhou 2003).

Southerly or southwesterly LLJs frequently occur in South China during the presummer rainy season (Du et al. 2014; Du and Chen 2019b). The LLJs in South China can be further classified into two types based on their characteristics and formation mechanisms: boundary layer jets (BLJs) and synoptic system–related low-level jets (SLLJs; Du et al. 2014; Du and Chen 2019b). The southerly BLJs are frequently observed in Beibu Gulf (around 20°N, 108°E) and the northern South China Sea, featuring pronounced diurnal variation with a

Corresponding author: Yu Du, duyu7@mail.sysu.edu.cn

DOI: 10.1175/JCLI-D-21-0121.1

nocturnal wind maximum at 950 hPa (Du and Chen 2019b). The formation mechanisms of the BLJs over inland South China are mainly influenced by boundary layer processes (Du et al. 2014; Du and Chen 2019b), which can be explained by the combination of inertial oscillation (Blackadar 1957) and diurnal thermal forcing on elevated topography (Holton 1967). On the other hand, the maximum occurrence frequency of the southwesterly SLLJs is found farther north over inland areas of South China. The SLLJs often appear at 850–700 hPa in the early morning and develop in response to the synoptic weather systems (Chen and Yu 1988; Du et al. 2014; Du and Chen 2019b).

The different roles of the BLJ and SLLJ on heavy rainfall have been noticed recently. The BLJs are found to be more associated with the coastal rainfall through interacting with coastal terrain (X. Chen et al. 2017; Du and Chen 2019a; Du et al. 2020a,b), land–sea thermal contrast (X. Chen et al. 2017; Wu et al. 2020), or differential friction of the underlying surface (X. Chen et al. 2017; Zhang and Meng 2019; Li et al. 2020; Du et al. 2020a,b). In contrast, the SLLJ can enhance inland rainfall near the front via colliding with the northerly cold dry flow (Du and Chen 2018; Li et al. 2020). Sometimes, the coupling of the double LLJs (simultaneous occurrence of the BLJ and SLLJ; Du et al. 2012; Du and Chen 2019a; Zhang and Meng 2019) promotes the initiation of coastal WR through low-level convergence at the terminus of the BLJ as well as midlevel divergence in the entrance of the SLLJ (Du and Chen 2019a; Li et al. 2020). The two types of LLJs also differ in moisture transportation (Du and Chen 2019b) and then influence the accumulated rainfall amount (X. Chen et al. 2017). There is preferential moisture transportation to the coastal rainfall by the BLJ and the inland rainfall by the elevated SLLJ (Du and Chen 2019b).

Although the close relationship between LLJs and heavy rainfall has been illustrated in many previous case studies, systematic studies in a statistical manner are still lacking. The quantitative responses of different types of heavy rainfall (including WR and FR) to varying BLJ or SLLJ are not yet well understood. Therefore, the objective of the present study is to examine the roles of two types of LLJs in different types of heavy rainfall over South China based on the statistics as an extension of the case study conducted by Du and Chen (2018, 2019a). We intend to address the following key questions: 1) What are the differences and similarities in the statistical relationships between the two types of heavy rainfall and LLJs over South China, including their diurnal variation, occurrence frequency, spatial pattern, and relative location? 2) How and why do their relationships vary with different locations in South China? The paper is organized as follows: The data and statistical methods used in the present study are introduced in section 2. Section 3 compares the two types of heavy rainfall in South China. Section 4 further presents the relations between the two types of heavy rainfall (WR and FR) and LLJs (BLJ and SLLJ) in detail. The results are summarized in section 5.

2. Data and methodology

a. Data

The 0.25° × 0.25° gridded rainfall data derived from Tropical Rainfall Measuring Mission 3B42V7 (TRMM; Huffman et al. 2007) are used in this study to provide the rainfall estimates at 3-h interval. In addition to long-term observations that facilitate climatological studies, TRMM performs well in resolving the features of warm season precipitation over China (Shen et al. 2010). The rationale behind using TRMM rainfall data is that they better characterize the diurnal cycles of rainfall over South China than CMORPH, which has been documented in Chen et al. (2018). In addition, meteorological variables are derived from the fifth generation of the European Centre for Medium-Range Weather Forecasts (ECMWF) atmospheric reanalyses (ERA5) with a horizontal spatial resolution of 0.25° × 0.25° on 37 pressure levels for identifying LLJs and diagnosing environmental conditions. Even though ERA5 is available at a high temporal resolution of 1 h, ERA5 data at 0000, 0300, 0600, 0900, 1200, 1500, 1800, and 2100 UTC are employed in the present study in order to coordinate with the TRMM precipitation availability. The period used in the present study of TRMM rainfall data and ERA5 reanalysis covers from April to June for 1998–2019, which is the presummer rainy season in South China.

b. Identification of rainfall types

The rainfall regions focused on in this study cover South China, including Guangxi and Guangdong provinces (~104°–118°E, 20°–27°N). Given that heavy rainfall affected by MCSs typically generates a large amount of precipitation in a short period, a heavy rainfall event is identified when 3-h accumulative rainfall (0000–0300, 0300–0600, 0600–0900, 0900–1200, 1200–1500, 1500–1800, 1800–2100, and 2100–0000 UTC) at one grid point equals or exceeds 30 mm in the study regions. The identification is on an event basis with a fixed 3-h time window; for example, heavy rainfall occurs during 0300–0600 and 0600–0900 UTC on the same day would be counted twice and considered as two independent heavy rainfall events. To examine the sensitivity of the identification, we tried a different time window in the definition of a heavy rainfall episode (6-h accumulative rainfall ≥ 30 mm) and found good consistency in the rainfall patterns between the two criteria. The 3-h time interval for a heavy rainfall event is used in the present study to be consistent with the TRMM data, which provide more detailed information on rainfall diurnal cycles. Additionally, heavy rainfall events influenced by tropical systems (e.g., typhoon) on the same day are excluded.

A total of 3898 heavy rainfall events are identified during the presummer rainy seasons (April–June) for 1998–2019 and then they are categorized as WR and FR types according to whether they occur in weak or strong synoptic-scale environments. The presummer rainy season behaves as a transitional period under the influence of the strengthened tropical warm moist flow and the weakened cold air from midlatitude systems (e.g., Huang 1986; Ding 1994; Li et al. 2020), both of which act on the formation of heavy rainfall. Sometimes the strong warm moist flow is dominant in rainfall production through interacting with other local forcings (e.g., coastal terrain, cold pool, etc.), which behaves as WR. Sometimes the southward intrusion of cold air or a front (interaction between cold and warm air) dominates, and the convection manifests as FR. The specific classification of the two types of heavy rainfall follows the method described

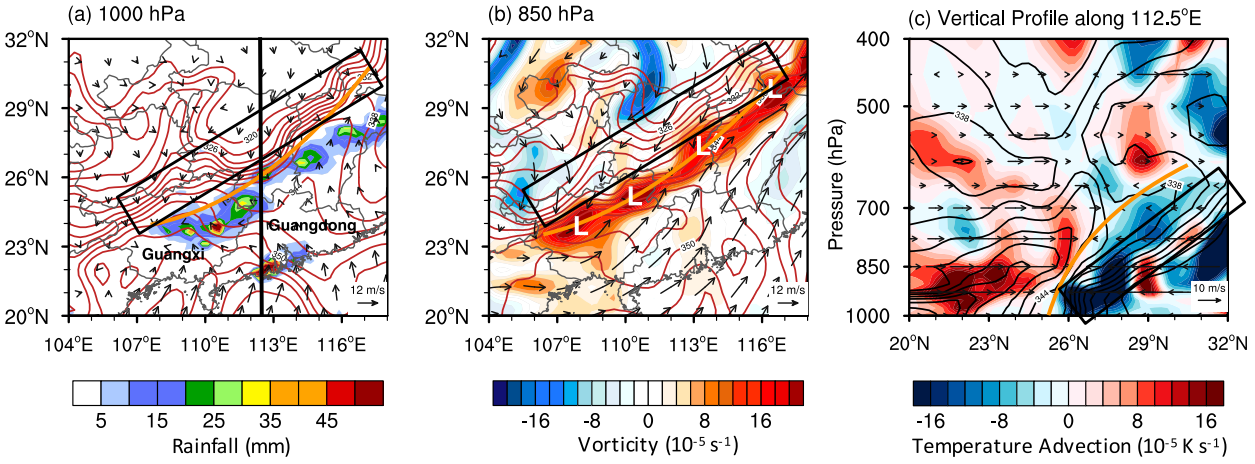

FIG. 1. Methodology to identify WR and FR with the example case of 2100 UTC 10 May 2014. (a) 3-h cumulative rainfall (shading; mm) and pseudoequivalent potential temperature at 1000 hPa (θ_{se}; red contour with an interval of 3 K), superimposed with 1000-hPa horizontal wind vectors (m s^{-1}). (b) Vorticity at 850 hPa (shading; 10^{-5} s^{-1}; letter L denotes a low pressure vortex), θ_{se} at 850 hPa (red contour with an interval of 3 K), and horizontal wind vectors at 850 hPa (m s^{-1}). (c) Vertical–meridional cross section of temperature advection (shading; 10^{-5} K s^{-1}), θ_{se} (black contour with an interval of 3 K), and meridional wind vectors (m s^{-1}) along the black solid line (112.5°E) marked in (a). The orange solid lines and black boxes represent the locations of fronts and dense belts of θ_{se}.

in Huang (1986) and Liu et al. (2019). WR occurs more than 200 km away from a front or in an area dominated by low-level southerly flows without a front. The scale of distance defined here (200 km) is based on climatological frontal activities, so that a WR event is less influenced by the front. On the other hand, heavy rainfall within 200 km away from the front is identified as the FR type.

According to the definition of WR and FR above, FR is closely associated with synoptic fronts, while WR is not affected by fronts and with weak synoptic-scale forcing. Therefore, the critical step in the classification is to examine whether the heavy rainfall is influenced by the fronts, which are often featured by high gradient zones of pseudoequivalent potential temperature (θ_{se}) with the occurrences of large convective instability (Xie 1956). An example case characterized by double rainbands at 2100 UTC 10 May 2014 (Fig. 1) is used to illustrate the classification procedure of heavy rainfall. Horizontal distributions of related meteorological variables (e.g., θ_{se}, winds, and vorticity) at 1000 and 850 hPa are examined first. A southwest–northeast-oriented dense belt of θ_{se} (black box) located in northern South China can be observed at both 1000 and 850 hPa, where a shear line (characterized by pronounced wind shear; orange solid line) appears near the dense belt of θ_{se} (Figs. 1a,b). Additionally, low pressure vortexes (labeled L) at 850 hPa are collocated with the shear line and a southwesterly SLLJ is embedded in the southeastern side of the low pressure vortexes (Fig. 1b). Since the dense belts of θ_{se} near the surface may be influenced by the terrain, the vertical meridional cross section along the heavy rainfall center (rainfall maximum; black line along 112.5°E in Fig. 1a) is additionally analyzed following Liu et al. (2019) in order to confirm the vertical incline structure of the front (Fig. 1c). A dense zone of θ_{se} occurs at 25°N at 1000 hPa and extends northward to above 700 hPa (32°N), indicating a front with a northward tilt. Wind shear is pronounced near the front, and cold/warm temperature advection occurs on either side of it. Southerly winds associated with warm air advection occur on the south side while northerly winds associated with cold air advection are on the north side. Based on the horizontal and vertical analyses above, the location of the front is identified and determined in northern South China as the orange solid lines in Fig. 1. According to the distance between the rainfall center and the front in the horizontal analyses, the rainband in northern Guangxi located near the front is classified into FR type, while the coastal rainband (around 22°N, 112.5°E in Guangdong) at a distance of greater than 200 km from the front is WR.

The method above is applied for the classification of each heavy rainfall event. Among 3898 heavy rainfall episodes, 1079, 2220, and 599 episodes are classified into WR, FR, and DR (double rainband) types, respectively. The DR type indicates that both WR and FR occur simultaneously in South China. It can be seen that most of the heavy rainfall (WR or FR) over South China occurs on its own. To clearly compare the features of WR and FR, we only focus on the episodes of WR and FR types considering the relatively low occurrence frequency in the DR type. Compared to similar previous studies concerning WR and FR in South China (e.g., Liu et al. 2019; Zhang and Meng 2019; Wu et al. 2020), the present study considers larger regions with higher-resolution reanalysis data and more objective classification method of heavy rainfall.

c. *Identification of LLJs*

In climatology, most of the BLJs exhibit southerly wind maxima at 950 hPa in South China, while the wind speed maxima of southwesterly SLLJs are most frequently found between 850 and 700 hPa (Du and Chen 2019b). Considering the mean height of LLJ occurrences, Zhang and Meng (2019) defined the LLJs by horizontal wind speed maximum at typical pressure levels irrespective of vertical wind shear, as in the regular operational synoptic analysis in southern China. The criteria defined by Zhang and Meng (2019) are basically

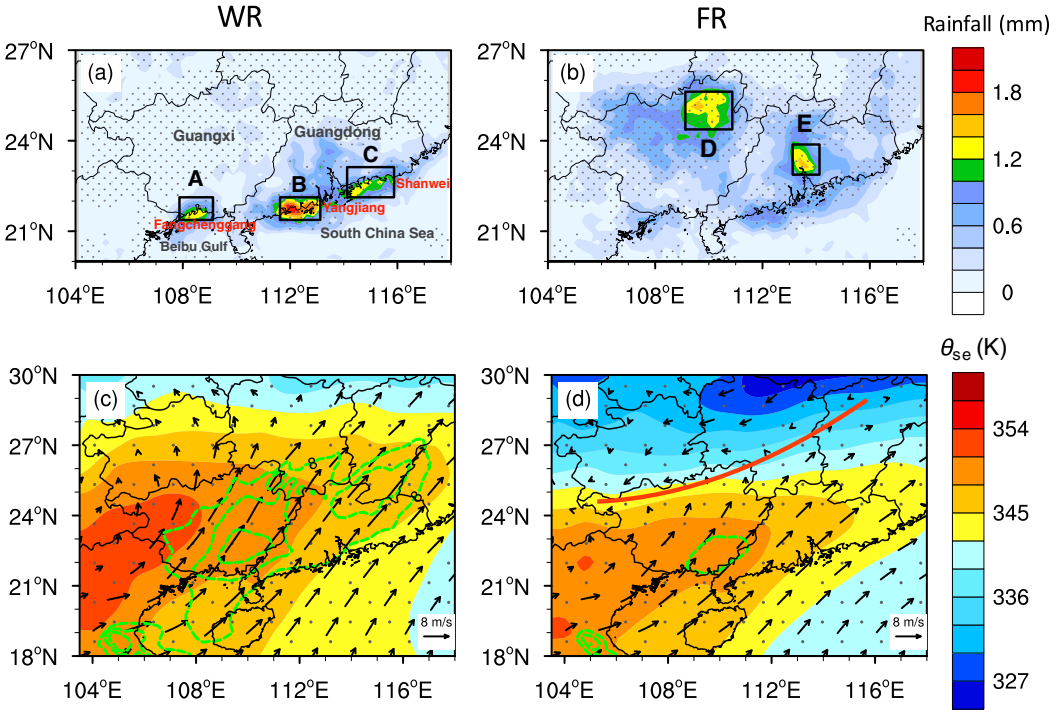

FIG. 2. Distributions of (a),(b) 3-h cumulative rainfall (mm) and (c),(d) environmental background including θ_{se} (shading; K), wind speed (green contour $\geq 8\ m\ s^{-1}$ with an interval of $1\ m\ s^{-1}$), and wind vectors at 850 hPa during the (left) WR and (right) FR events. The black boxes indicate three coastal WR centers marked as regions A, B, and C in (a) and two inland FR centers marked as regions D and E in (b). The red solid line in (d) indicates the location of a front. The dots indicate the area where the difference of composite 3-h cumulative rainfall [in (a) and (b)] and θ_{se} [in (c) and (d)] between WR and FR events are significant above the 90% level by two-tailed Welch's t test.

applied in the present study since we pay more attention to the horizontal structures of LLJs. However, we tried to eliminate the influence of strong upper-level winds on the identification of LLJs, so an additional criterion of vertical wind shear above the levels of LLJs is added. Since the wind speed at 850 hPa is generally larger than that at 950 hPa on average, the thresholds we chose are varied for the BLJ and SLLJ. The BLJ is identified as the full wind speed maximum at 950 hPa larger than or equal to $10\ m\ s^{-1}$, and the wind speed at the jet core (the location of maximum wind speed) greater than that at 850 hPa. The SLLJ is defined as full wind speed maximum of $12\ m\ s^{-1}$ or greater at 850 hPa, and when the wind speed at the jet core exceeds the wind speed at the corresponding location of 700 hPa. Additionally, only LLJs with wind directions between 90° and 270° that have southerly wind components are considered.

d. Identification of heavy rainfall associated with LLJs

To facilitate the discussion on the relations between heavy rainfall and LLJs, we examined the presence of LLJs at the beginning of the 3-h rainfall event. If only the BLJ (SLLJ) occurs in the range of 200 km from the heavy rainfall center, the heavy rainfall event is considered as a BLJ (SLLJ) event (Zhang and Meng 2019). In addition, heavy rainfall events associated with either the BLJ or SLLJ are classified as LLJ events, while heavy rainfall events associated with neither the BLJ nor SLLJ are classified as non-LLJ events. Heavy rainfall events associated with both the BLJ and SLLJ simultaneously are considered as double-LLJ (DLLJ events. To obtain robust results in this study, statistical significance tests are conducted. The correlations between heavy rainfall and LLJs discussed in section 4b are significant at the 99% confidence level by two-tailed Student's t test. The composited spatial distributions are significant at the 90% confident level by two-tailed Welch's t test, which is used to compare the differences of various atmospheric variables between WR and FR events in section 3 (LLJ and non-LLJ events or regional WR/FR and total WR/FR events in section 4).

3. Features of warm-sector and frontal heavy rainfall

To better understand the relationships between heavy rainfall and LLJs, the general characteristics of the two types of heavy rainfall (WR and FR) over South China are first compared in this section.

a. Spatial distribution

The climatological spatial distributions of 3-h accumulative rainfall in WR and FR are compared in Figs. 2a and 2b. Generally, WR and FR differ from each other in their locations and distributions. WR shows maximum centers along the

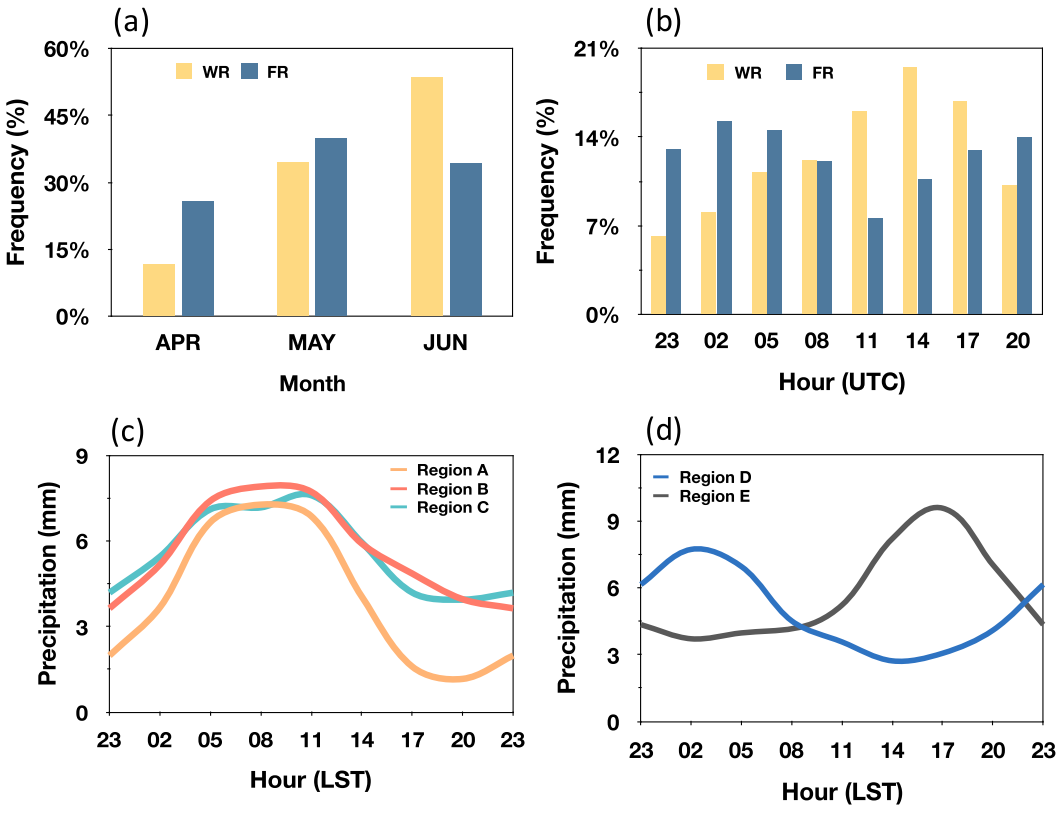

FIG. 3. (a) Monthly and (b) diurnal variations of the occurrence frequencies (%) of WR and FR episodes over South China. (c) Diurnal variations of 3-h region-averaged rainfall (mm) during the regional WR days over regions A, B, and C (black boxes shown in Fig. 2a). (d) Diurnal variations of 3-h region-averaged rainfall (mm) during regional FR days over regions D and E (black boxes shown in Fig. 2b).

coastline, located in Fangchenggang of Guangxi (region A), Yangjiang of Guangdong (region B), and Shanwei of Guangdong (region C). In contrast, the centers of FR occur over inland regions, concentrating in the north of Guangxi (region D) and central Guangdong (region E). In addition, the spatial distributions of occurrence frequencies of WR and FR events (not shown) correspond well to the 3-h accumulative rainfall patterns.

b. *Environmental background*

The differences in the composite analyses of environmental fields between WR and FR are shown at the onset time of heavy rainfall events in Figs. 2c and 2d. In WR, strong southwesterly winds at 850 hPa ($\geq 8\,\mathrm{m\,s^{-1}}$, indicated by the green contours) prevail over South China (Fig. 2c). But the winds in FR are much weaker at 850 hPa (Fig. 2d). Accordingly, the high θ_{se} tongue in WR can penetrate farther north in contrast to that in FR, implying a much warmer and moister environment in WR. In addition, a front (convergence line with large thermal contrast, red solid line) exists in the north of South China in FR (Fig. 2d), while WR is present under weak synoptic forcing (Fig. 2c).

c. *Monthly and diurnal variations*

The monthly and diurnal variations of WR and FR are further compared in Fig. 3. The occurrence frequency of WR events exhibits a pronounced monthly variation and significantly increases after the onset of the summer monsoon in June (Fig. 3a). However, FR events often occur in May when it is frequent for the convergence of southerly warm-moist and northerly cold dry air masses (Fig. 3a).

Given the discrepancies between the spatial distributions of WR and FR (Figs. 2a,b), we further divide the rainfall centers into three coastal WR-subregions and two inland FR-subregions shown in the black boxes of Fig. 2. Regional WR (FR) events are thus identified when WR (FR) events occur only in those concerned regions (regions A–C or D and E). To study the diurnal cycles of rainfall, we further define regional WR (FR) days as when at least one regional WR (FR) event occurs in the concerned region in a day. Following the criteria described above, 108 (79), 162 (97), and 191 (103) regional WR events (days) appear in regions A, B, and C, respectively. Similarly, there are 494 (264) and 304 (160) regional FR events (days) identified in regions D and E.

The differences in diurnal variations of rainfall are further explored among different regions. During the regional WR days, all the three coastal WR centers (regions A, B, and C) reach their rainfall peaks in the early morning around 0500–1100 LST (2100–0300 UTC; LST = UTC + 8 h; Fig. 3c). However, the occurrence frequency of WR events over South China peaks over 1100–1700 LST (0300–0900 UTC; Fig. 3b),

implying that the magnitude of WR is much higher in the early morning than in the afternoon. In comparison, the diurnal cycles of two inland FR centers are distinct from each other (Fig. 3d). In region D, strong rainfall intensity is found at night (0200–0500 LST; 1800–2100 UTC as well), which is possibly attributed to the eastward propagating of MCSs formed over the Yunnan–Guizhou Plateau in the afternoon (Jiang et al. 2017; Chen et al. 2018). On the other hand, rainfall in region E reaches its maximum in the afternoon around 1700 LST due to the solar heating effect (Wu et al. 2020; Chen et al. 2018). The occurrence frequency of FR events in South China presents a nocturnal peak over 0200–0500 LST (1800–2100 UTC; Fig. 3b), which may be mostly attributed to the diurnal variation of the FR events in region D. In general, large variations in the background environment result in significant differences in the diurnal variations of WR and FR. Further analysis and discussion on the early morning rainfall peak of WR will be given in the next section.

4. The relationships between heavy rainfall and LLJs

After the investigation into the two types of heavy rainfall in South China, relations between the two types of heavy rainfall and LLJs are further discussed in the present section including their diurnal variation, occurrence frequency, spatial pattern, and relative location.

a. Diurnal variations of LLJs and heavy rainfall

Previous studies (e.g., X. Chen et al. 2017; Xue et al. 2018; Zhang et al. 2019) have documented that the accumulated moisture (net moisture fluxes) in the boundary layer is a key factor of the diurnal cycle of rainfall. Thus, to investigate the primary cause of the early morning peak of WR, we first examine the diurnal variations of moisture fluxes into the three WR subregions (regions A–C; black boxes in Fig. 2a). The low-level moisture fluxes through four boundaries are calculated based on

$$Q = -\frac{1}{g}\int_{P_{1000}}^{P_{850}}\int_{x_1}^{x_2}(qV)\,dx\,dp, \tag{1}$$

where g, q, and V are gravity acceleration, specific humidity, and wind velocity perpendicular to the boundary, respectively. The term Q indicates the integral of moisture fluxes over the length of the boundary from x_1 to x_2, and from 1000 up to 850 hPa. The flux directed into the region is positive and the sum of the fluxes over the four boundaries represents the net moisture flux that converges into the region.

Figure 4 presents the low-level moisture fluxes through four boundaries of the three regional WR centers as well as net moisture fluxes during the regional WR days. In region A (Fig. 4a), the magnitudes of moisture fluxes through the southern and northern boundaries (yellow and blue dashed lines) are much larger than those through the western and eastern boundaries (gray and purple dashed lines) due to the prevailing southerly winds at low levels. When compositing the moisture fluxes through the southern and northern boundaries, the fluxes (red solid line) show a similar diurnal variation with the net moisture fluxes (black solid line), characterized by a maximum at 2300–0500 LST and a minimum at 1400 LST (Fig. 4a). In comparison, the composited moisture fluxes through the western and eastern boundaries (brown solid line) do not show a significant diurnal cycle. As mentioned in section 3c, the rainfall of WR over region A (green bars of Fig. 4a) peaks in the early morning (0500–1100 LST), which is about 6 h later than the net moisture flux peak (2300–0500 LST). Similar features in the diurnal variations of rainfall and moisture fluxes are observed in regions B and C (Figs. 4b,c).

Since the diurnal variation of net moisture fluxes is almost identical to the corresponding change of fluxes through the southern and northern boundaries, only fluxes through the southern and northern boundaries are analyzed in Fig. 5. Figure 5 shows the diurnal perturbation moisture fluxes (winds) at the low levels and corresponding divergence in the three WR subregions during the regional WR days. In region A, the diurnal variation of perturbation moisture fluxes is similar to that of perturbation winds (Figs. 5a,b), while the diurnal variation of specific humidity is not evident, but with high moisture concentrated in the boundary layer (not shown). The enhancement of low-level moisture transportation through the southern boundary occurs during 2300–0500 LST (Fig. 5a), which is attributed to the nocturnal strengthened BLJ and high specific humidity at low levels. In contrast, the strongest outward moisture fluxes from the northern boundary are also found over 2300–0500 LST extending from 975 to 850 hPa due to the prevailing southerly winds (Fig. 5b). It is also noted that shallow moisture inflow occurs below 975 hPa on the northern boundary during this time, corresponding to the land breeze that occurs in the land earlier than the sea (X. Chen et al. 2017). The coupling of the BLJ and land breeze enhances the convergence over 2300–0500 LST below 975 hPa (Fig. 5c) and accumulates moisture in region A by enhancing the inflow and weakening the outflow, thereby contributes to the nocturnal net moisture flux peak (Fig. 4a).

Similar analyses are conducted in regions B and C (Figs. 5d–i) and show consistent diurnal variations of perturbation winds and convergence with peaks at 2300–0500 LST in modulating the diurnal variations of moisture fluxes. To elucidate the thermodynamic forcing for the early morning rainfall peak of WR, we further investigate the diurnal variation of convective available potential energy (CAPE; not shown). CAPE decreases from 2300 to 0800 LST with a minimum at 0800 LST, and then starts to increase with a peak at 1400 LST, which might be affected by solar radiation. To some extent, the increased CAPE in the early morning (0800–1100 LST) contributes to the maintaining of the rainfall peak. However, rainfall weakens quickly after 1100 LST despite increased CAPE. Therefore, the thermodynamic effects (CAPE) on the diurnal variation of WR are limited.

b. Occurrence frequency of heavy rainfall associated with LLJs

The relationship in occurrence frequency between WR (or FR) events and LLJs is investigated statistically. Figure 6a exhibits that 76% (62%) of WR (FR) events in South China are related to LLJs at the onset of the rainfall, whereas the

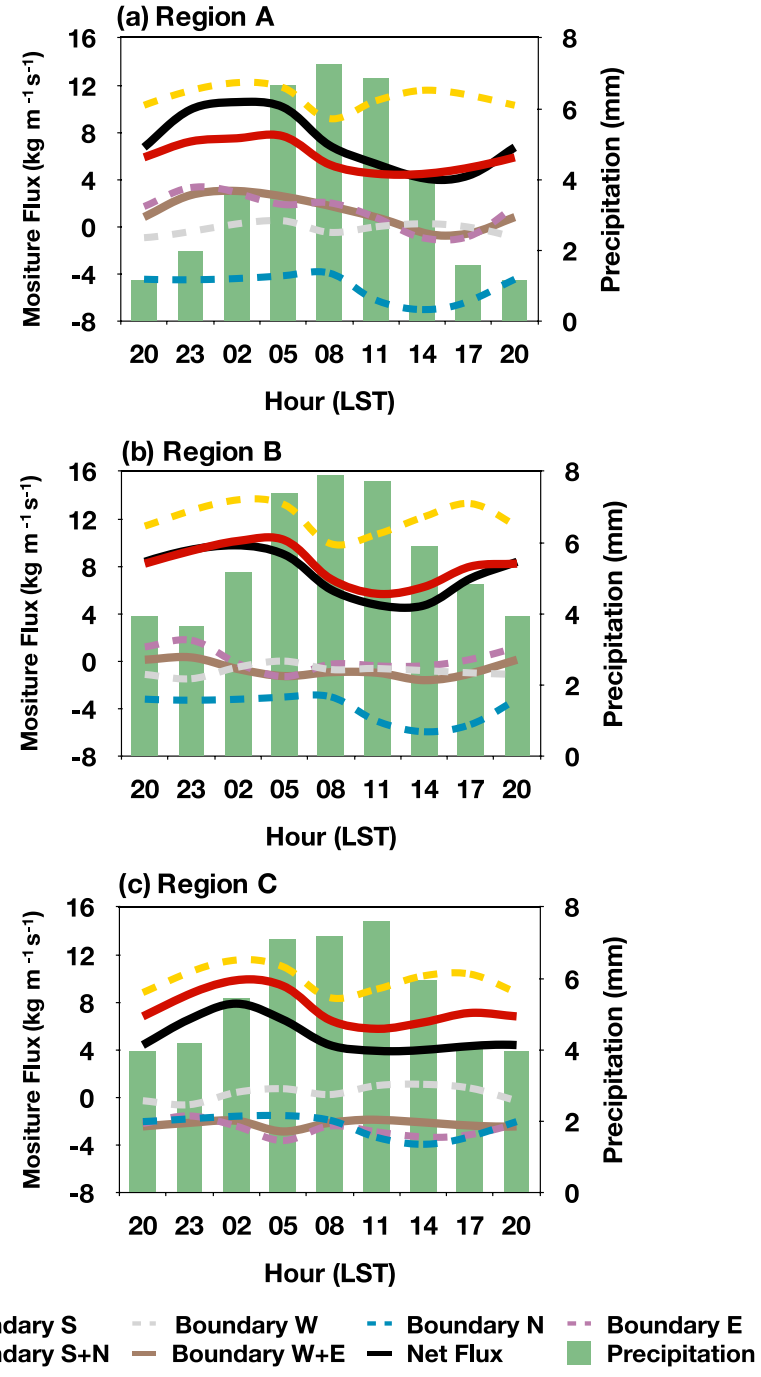

FIG. 4. Diurnal variations of low-level net moisture fluxes (black solid line; kg $m^{-1} s^{-1}$), moisture fluxes for boundary S (southern boundary; yellow dashed line), boundary N (northern boundary; blue dashed line), boundary W (western boundary; gray dashed line), boundary E (eastern boundary; purple dashed line), boundary S + N (red solid line), and boundary W + E (brown solid line), and 3-h region-averaged rainfall (green bar; mm) during the regional WR days over (a) region A, (b) region B, and (c) region C.

occurrence frequencies of WR and FR without LLJs are considerably lower (24% and 38%, respectively). DLLJ events account for more than half of heavy rainfall events associated with LLJs, reaching 47% in WR and lower in FR (32%). Therefore, WR in southern China is often accompanied by double LLJs (coexistence of BLJ and SLLJ), which has also been reported by Zhang and Meng (2019). The connections between LLJs and two types of heavy rainfall on monthly and

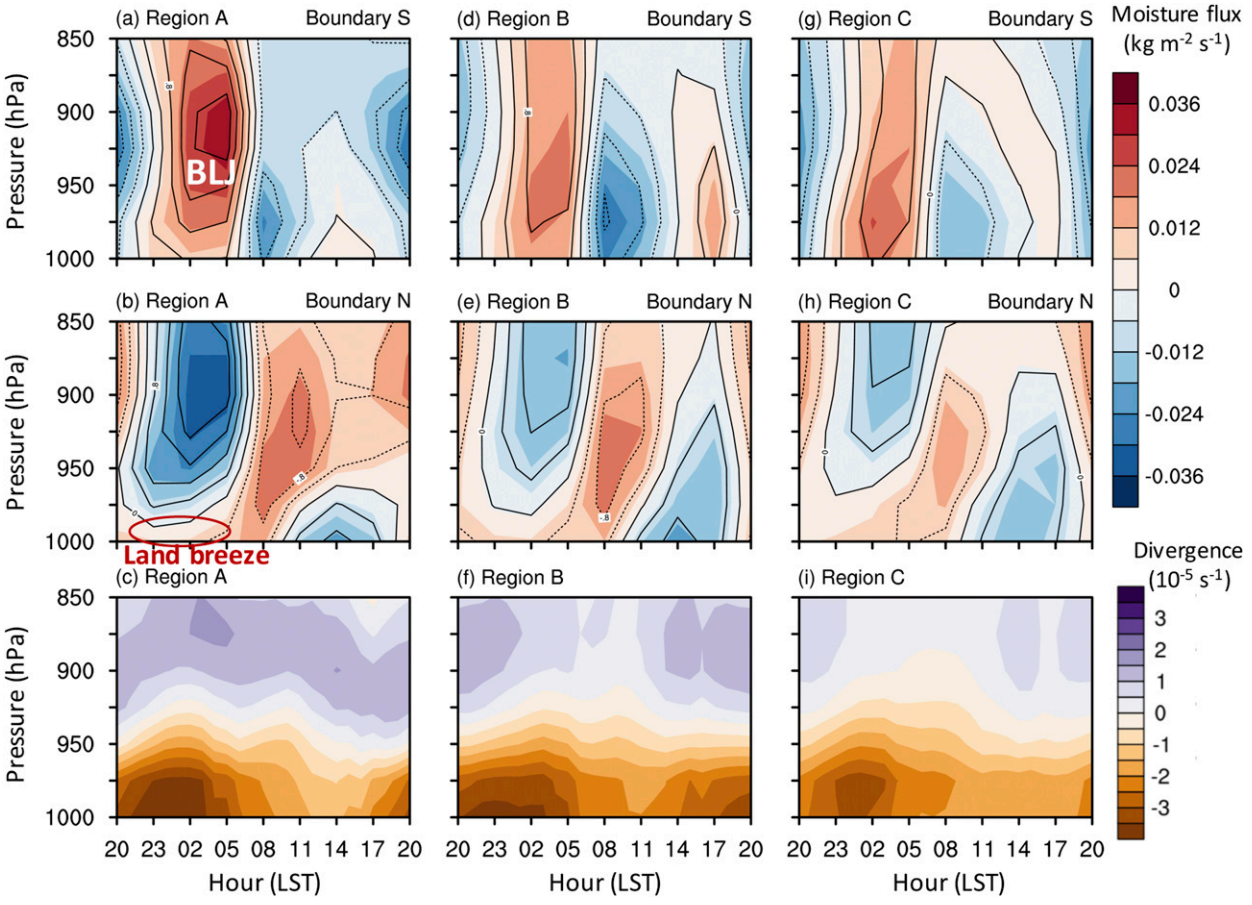

FIG. 5. Diurnal variations of composite boundary-averaged perturbation moisture fluxes (shading; kg m^{-2} s^{-1}) and perturbation winds (contoured every 0.4 m s^{-1}) through (top) boundary S, (middle) boundary N, and (bottom) region-averaged divergence (10^{-5} s^{-1}) during the regional WR days over (a)–(c) region A, (d)–(f) region B, and (g)–(i) region C. The diurnal perturbations (moisture fluxes or winds) are calculated by subtracting the daily mean during the regional WR days. The fluxes directed into (outward off) the region are positive (negative). The solid (dashed) contours indicate perturbation southerly (northerly) winds.

diurnal scales are further discussed. The heavy rainfall events associated with LLJs occur with higher contribution ratios than the non-LLJ events on both monthly and diurnal scales (Figs. 6b,c), particularly in WR, which indicates closer relationships between LLJs and WR than FR. The contribution of LLJ-WR events to total WR events reaches 88%–92% in the early morning (0200–0800 LST; Fig. 6c), which may be modulated by the diurnal variations of BLJ with a nocturnal peak (Du and Chen 2019b). The contribution percentage of non-LLJ events starts to increase in the daytime and peaks in the afternoon (1400–2000 LST; Fig. 6c), suggesting favorable thermodynamic conditions for heavy rainfall.

In the existence of LLJs, the rainfall intensity in WR or FR (LLJ-WR or LLJ-FR events) is much stronger compared to the climate mean state (cf. Figs. 7a,b and 2a,b). In contrast, the rainfall in South China is comparatively weaker during the non-LLJ events (non-LLJ-WR and non-LLJ-FR events), without prominent rainfall centers in the absence of LLJs (Figs. 7c,d). These results indicate that the LLJs contribute to the total rainfall amount in both WR and FR substantially. In particular, DLLJ (DLLJ-WR and DLLJ-FR) events reproduce stronger coastal WR and inland FR (Figs. 7e,f) compared to the general LLJ events (Figs. 7a,b), accompanied by stronger coastal BLJs and inland SLLJs.

A more detailed comparison on the occurrence frequency of heavy rainfall related to different types of LLJs is presented in Fig. 8. It reveals that BLJs have a close relationship with both WR and FR, but with slightly higher occurrence frequency in WR events. In contrast, SLLJs occur more frequently during FR than in WR because the occurrences of SLLJs are synoptically driven in South China (Du and Chen 2019b). The related rainfall distributions show significantly different patterns between BLJ and SLLJ events (Fig. 9). WR events associated with BLJs (BLJ-WR events) are characterized by concentrated rainfall over the coastal areas (Fig. 9a) due to coastal lifting by BLJ interacting with other factors, which is distributed similarly as the climatological WR pattern (Fig. 2a). Winds at 850 hPa during BLJ-WR events include some signals about strong southwesterly flows but do not meet the SLLJ definition (Fig. 9a). Rainfall often occurs along the coastal area of Guangdong and central Guangdong during the BLJ-FR events (Fig. 9b). However, with weaker SLLJs, the inland FR center over northern Guangxi weakens and migrates southward (Fig. 9b).

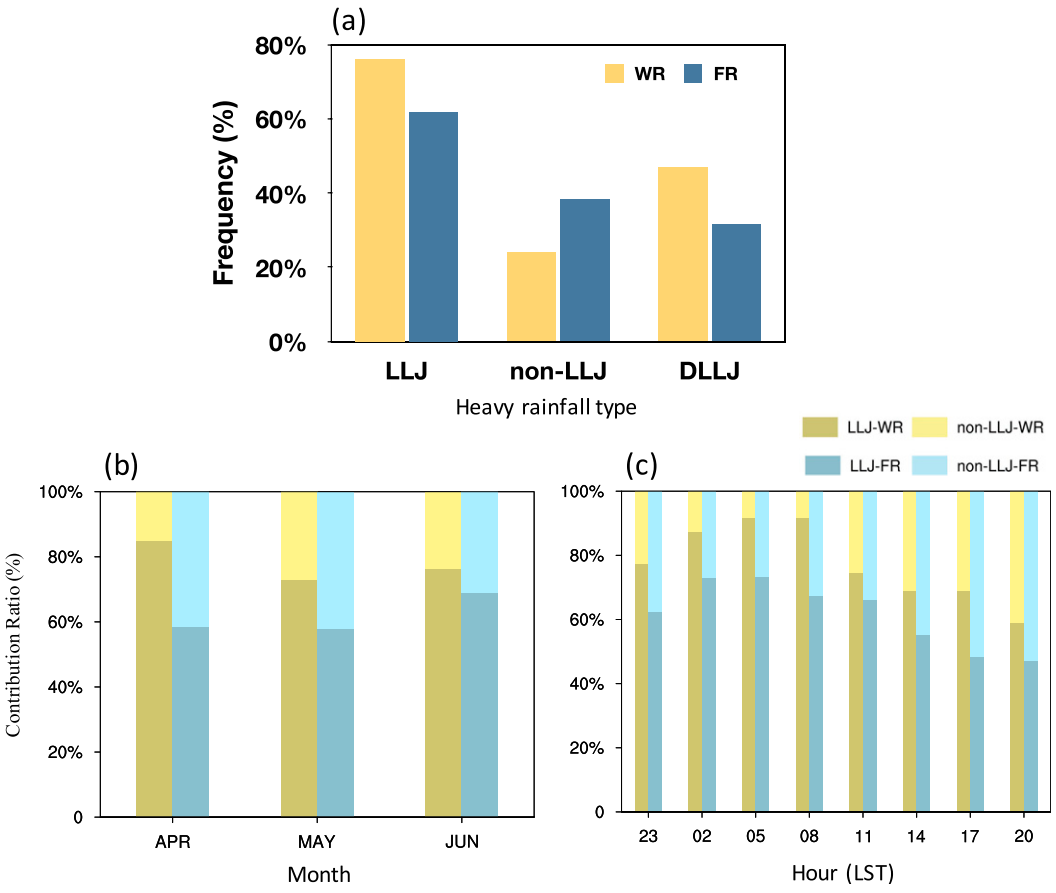

FIG. 6. (a) Occurrence frequencies (%) of WR (yellow bars) and FR (blue bars) events associated with LLJs, non-LLJs, and double LLJs at the onset of the rainfall over South China. The results are significant at the 99% confidence level by two-tailed Student's *t* test. (b) Monthly and (c) diurnal variations of the contribution ratio (%) of WR (yellow bars) and FR (blue bars) events associated with LLJs (dark bars) and non-LLJs (light bars).

Furthermore, WR events accompanied by SLLJs (SLLJ-WR events) show strong coastal heavy rainfall (Fig. 9c), but the centers shift to the east of the coastline in Guangdong when compared with the climatological rainfall pattern (Fig. 2a). As for the SLLJ-FR events, rainfall centers in northern Guangxi are present but the original rainfall center in central Guangdong is much weakened (Fig. 9d). Therefore, both BLJ and SLLJ show close relationships with coastal and inland rainfall.

c. Spatial pattern of LLJs associated with heavy rainfall

Besides occurrence frequency, the LLJ events also differ from the non-LLJ events in their dynamic and thermodynamic environments, especially in the LLJ structures. Figure 10 compares the composite perturbation environments during the LLJ-WR and non-LLJ-WR events. The composite perturbations are computed by subtracting the seasonal mean based on 1998–2019 during the presummer rainy season. The southerly low-level winds prevail over South China on seasonal average. During the WR events associated with LLJs, perturbation southwesterly winds occur over the land of South China at 850 hPa, corresponding to the SLLJ core located over southeastern Guangxi and northeastern Guangdong (Fig. 10a). At 950 hPa, stronger southerly perturbation winds, namely BLJs, exhibit two regional maxima: one over Beibu Gulf and the other over the northern South China Sea (Fig. 10c). Such wind distributions account for relatively strong convergence at low levels along the coastline (Fig. 10e), which is favorable for the warm-sector convection. The rising motion at low levels shows a similar pattern with strong convergence in the exit region of the BLJ (Fig. 10e). The enhanced CAPE is also evident along the coastline, which is driven shoreward by the strengthened southerly winds (Fig. 10g). In contrast, such favorable environmental conditions for WR become much weaker in the absence of LLJs (Figs. 10b,d,f,h) and thus suppress rainfall (Fig. 7c). For instance, perturbation winds at 850 and 950 hPa during non-LLJ-WR events are much weaker than those in the LLJ-WR events (cf. Figs. 10a–d), with reduced convergence, weaker rising motion (Fig. 10f), and lower CAPE (Fig. 10h) along the coastline accordingly. Higher convective inhibition (CIN) is observed in the coastal areas of Guangxi and western Guangdong in LLJ-WR events than in non-LLJ-WR events, while lower CIN distributes in the coastal regions of eastern Guangdong (Fig. 10g). Therefore,

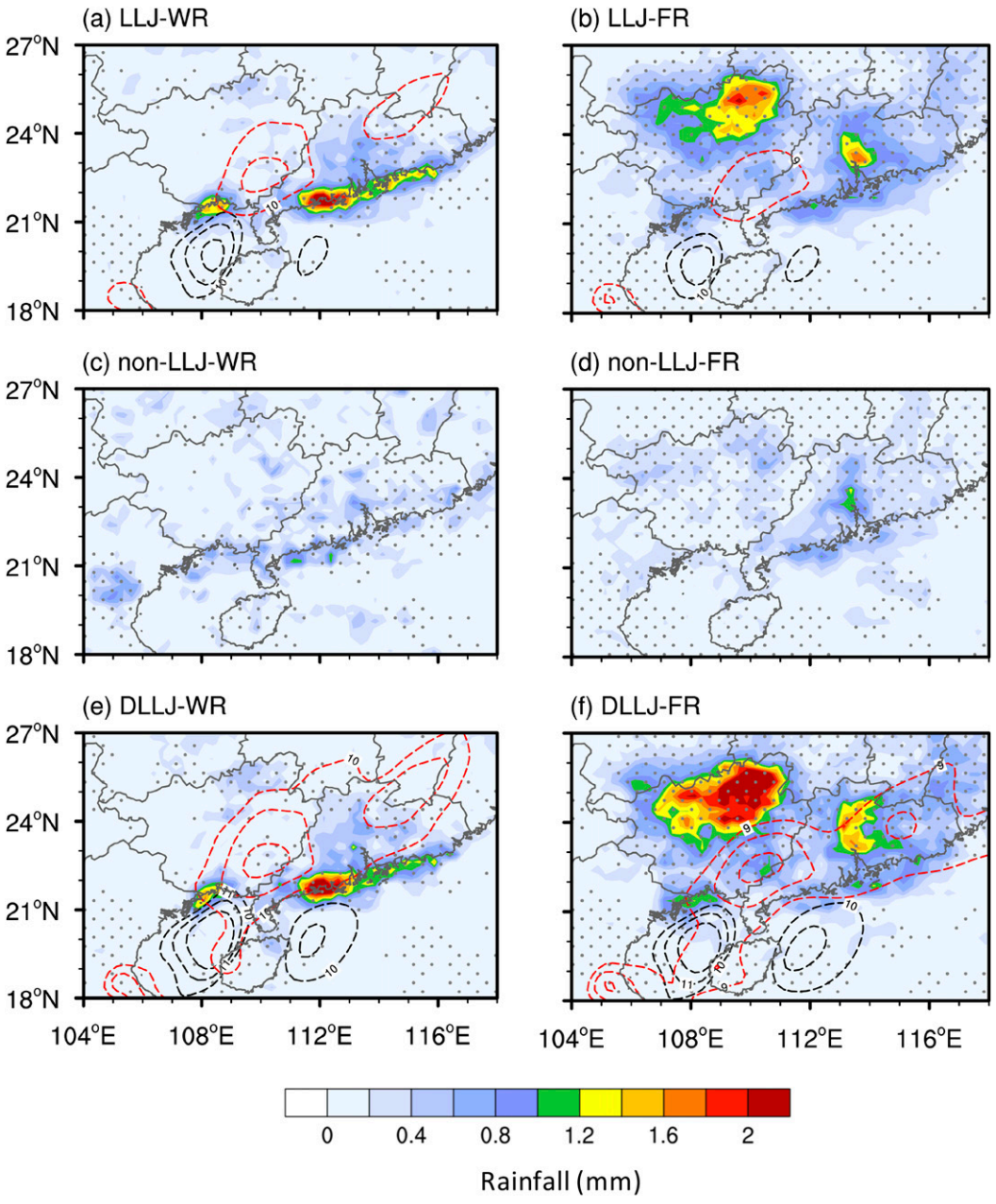

FIG. 7. Composite 3-h cumulative rainfall (mm) and horizontal wind speed at 850 hPa (red contour with an interval of 1 m s^{-1}) and 950 hPa (black contour with an interval of 1 m s^{-1}) during the (left) WR and (right) FR events associated with (a),(b) LLJs, (c),(d) non-LLJ, and (e),(f) double LLJs. The dots in (a) and (c) and (b) and (d) denote the area where the significance level of the difference of composite 3-h cumulative rainfall between LLJ and non-LLJ events is greater than 90% by two-tailed Welch's *t* test. The dots in (e) and (f) are same as (a) and (b), but between DLLJ and non-LLJ events.

the occurrences of LLJ-WR events are not necessarily accompanied by lower CIN.

Similar comparisons of environmental conditions between LLJ-FR and non-LLJ-FR events are further examined in Fig. 11. An evident shear line located in northern South China is observed during the LLJ-FR events but is absent during the non-LLJ-FR events at both 850 and 950 hPa (cf. Figs. 11a–d). Stronger southwesterly perturbation winds are embedded in the south of the front during the LLJ-FR events (Figs. 11a,c), corresponding to the inland SLLJs at 850 hPa and the oceanic BLJs at 950 hPa. Both the BLJs and SLLJs enhance the supply of moister and warmer air toward the inland areas. Contrastingly, the perturbation winds are weaker without a convergence between cold and warm air due to dominant northerly disturbances

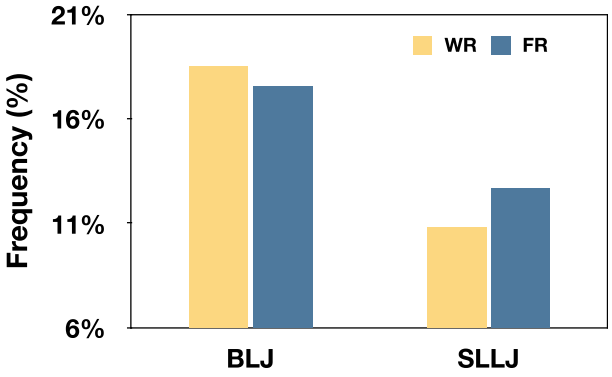

FIG. 8. As in Fig. 6a, but for BLJ and SLLJ events. The results are significant at the 99% confidence level by two-tailed Student's *t* test.

during the non-LLJ-FR events (Figs. 11b,d). Stronger convergence at 850 hPa occurs in northern Guangxi during the LLJ-FR events (Fig. 11e), which corresponds to one of the FR centers in region D (Fig. 2b). The strong rising motion at low levels matches the region with pronounced wind shear (Fig. 11e). Higher CAPE in South China is a consequence of stronger BLJ and SLLJ during the LLJ-FR events (Fig. 11g), which provides more favorable conditions for moist convection. In comparison, the non-LLJ-FR events show weaker low-level convergence and rising motion (Fig. 11f), and much lower CAPE (Fig. 11h). No significant difference in CIN is found between LLJ-FR events and non-LLJ-FR events in the region where FR prefers to occur (Fig. 11g). Therefore, LLJ occurrences tend to supply more moisture to the rainfall region, enhance low-level convergence, increase convective energy, and thus result in more intense rainfall. However, CIN is not clearly associated with rainfall anomalies.

We further discuss the subregional variability in the relationships between regional heavy rainfall and two types of LLJs under varying environmental conditions (Fig. 12). Regional heavy rainfall events are identified by the occurrence of heavy rainfall only in the concerned region (e.g., region A). Generally, the LLJs related to different regional rainfall vary in morphology, strength, and location. Compared to that of region A, the location of the SLLJ for the WR of region B is farther east (cf. Figs. 12b and 12a) and the BLJ in

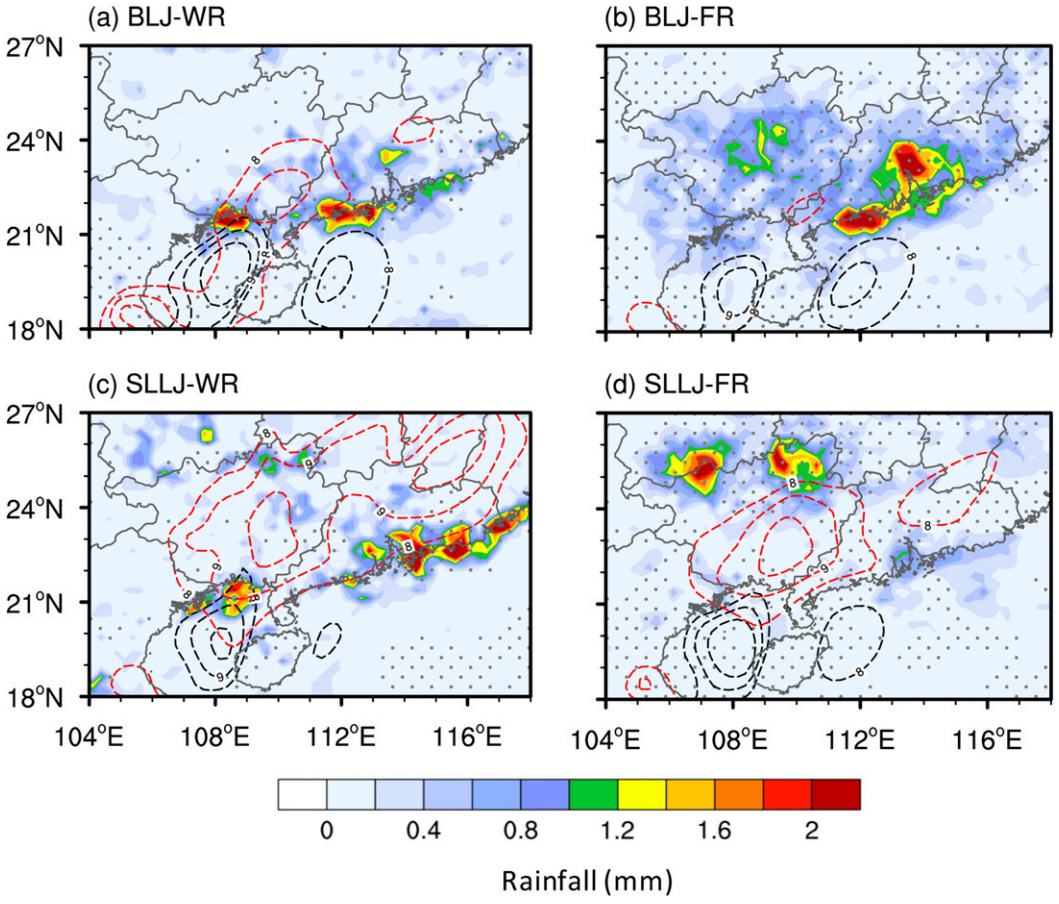

FIG. 9. As in Fig. 7, but for (a),(b) BLJ and (c),(d) SLLJ events. The dots in (a) and (b) denote the area where the significance level of the difference of composite 3-h cumulative rainfall between BLJ and non-LLJ events is greater than 90% by two-tailed Welch's *t* test. The dots in (c) and (d) are the same as in (a) and (b), but between SLLJ and non-LLJ events.

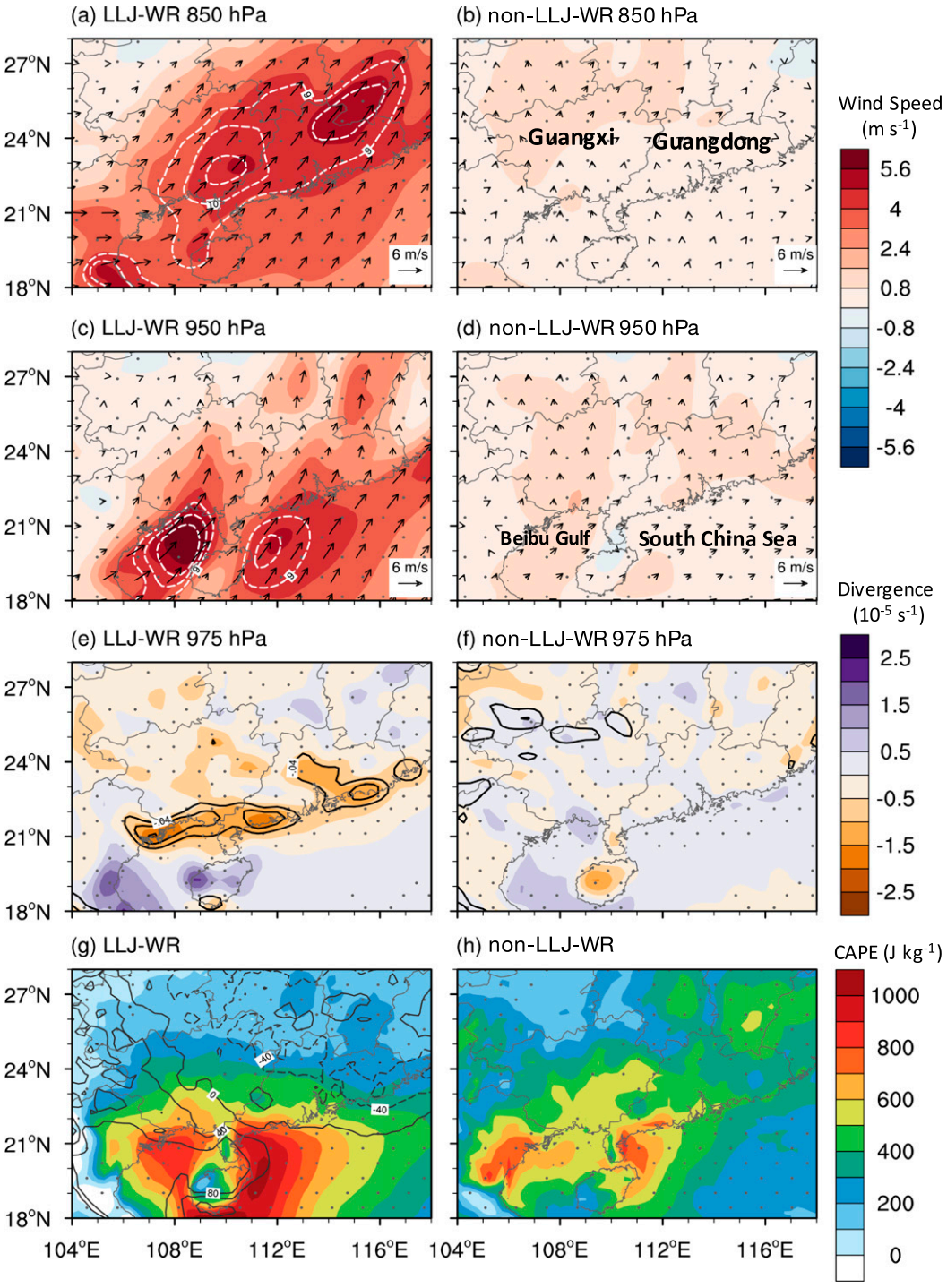

FIG. 10. Distributions of composite perturbation wind speed (shading; m s^{-1}), perturbation wind vectors, and horizontal wind speed (contour with an interval of 1 m s^{-1}) at (a),(b) 850 and (c),(d) 950 hPa, (e),(f) perturbation divergence (10^{-5} s^{-1}) and vertical velocity (contour with an interval of -0.02 Pa s^{-1}) at 975 hPa, and (g),(h) perturbation CAPE (J kg^{-1}) during the (left) LLJ-WR and (right) non-LLJ-WR events, superimposed with CIN difference between LLJ-WR and non-LLJ-WR events (contour with an interval of 40 J kg^{-1}). Positive (negative) CIN anomalies are plotted in solid (dashed) contours. The dots denote the area where the significance level of the difference of composite variables between LLJ-WR and non-LLJ-WR events is greater than 90% by a two-tailed Welch's *t* test.

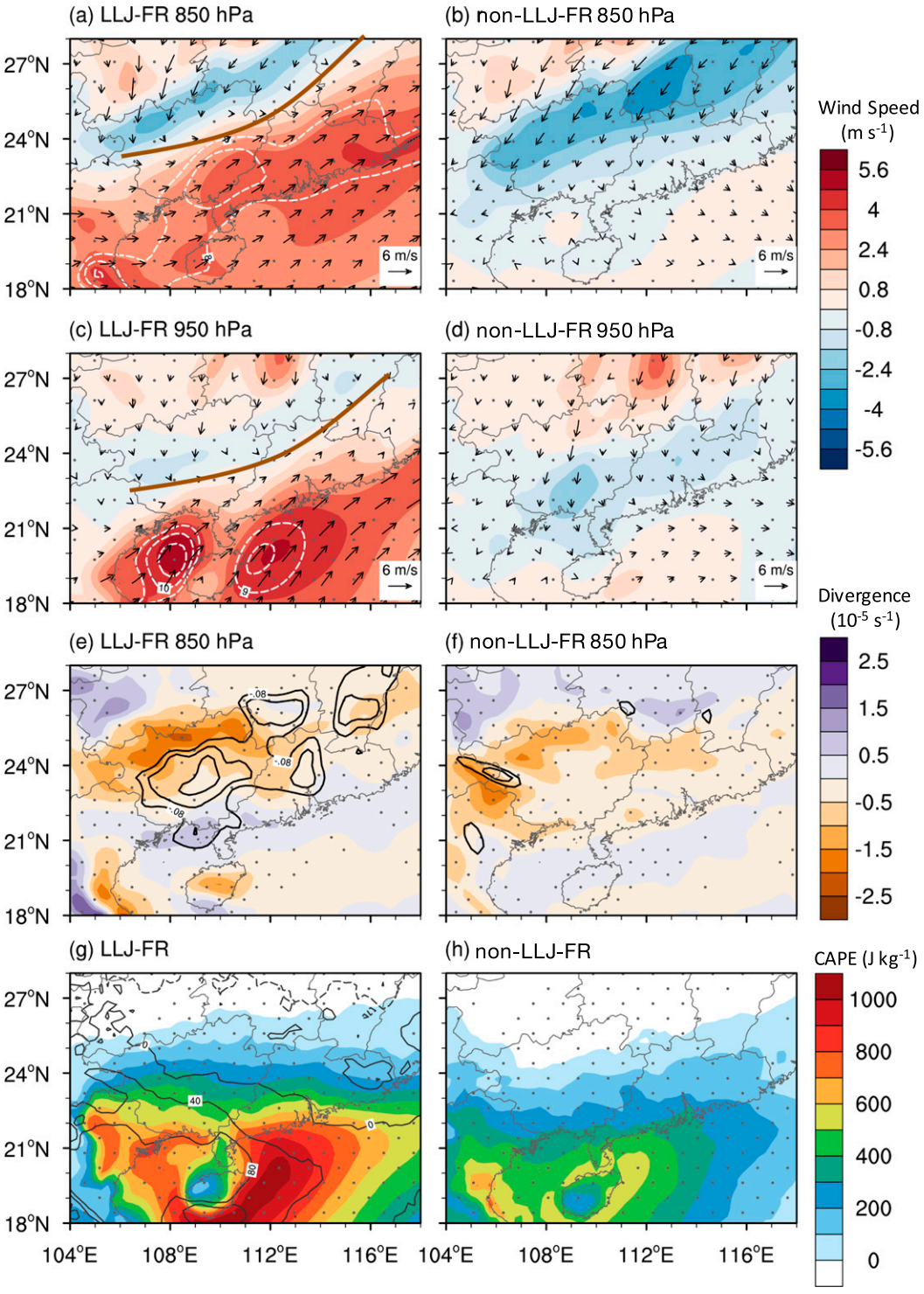

FIG. 11. As in Fig. 10, but for (a),(c),(e),(g) LLJ-FR events and (b),(d),(f),(h) non-LLJ-FR events. Note that (e) and (f) are at 850 hPa; the brown lines in (a) and (c) indicate the locations of a front at 850 and 950 hPa. The dots denote the area where the significance level of the difference of composite variables between LLJ-FR and non-LLJ-FR events is greater than 90% by two-tailed Welch's *t* test.

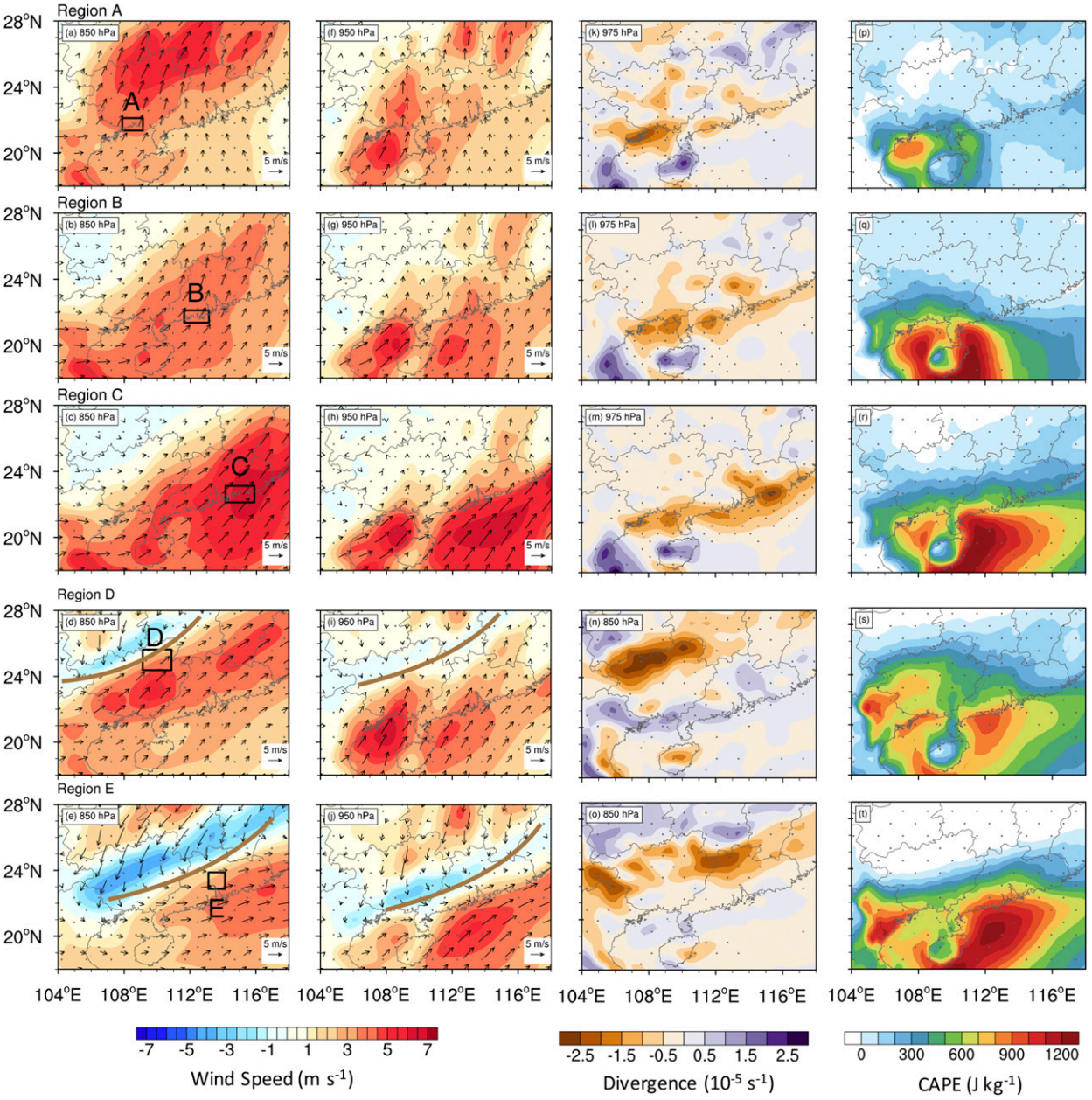

FIG. 12. The three top rows are as in Fig. 10, but for the regional WR events of (a),(f),(k),(p) region A, (b),(g),(l),(q) region B, and (c),(h),(m),(r) region C. The remaining two rows are same as Fig. 11, but for the regional FR events of (d),(i),(n),(s) region D and (e),(j),(o),(t) region E. The black boxes in (a)–(e) indicate regional rainfall centers marked as regions A–E in Fig. 2. The brown lines in (d), (e), (i), and (j) indicate the locations of fronts at 850 and 950 hPa. The dots denote the area where the significance level of the difference of composite variables between regional WR (FR) events and total WR (FR) events is greater than 90% by two-tailed Welch's *t* test.

the area upstream of region B, over the northern South China Sea, is stronger (cf. Figs. 12g and 12f). As for WR in region C, wider and stronger SLLJ and BLJ extend farther eastward (Figs. 12c,h). The two types of LLJs also manifest as larger westerly wind components, which are beneficial for transporting more water vapor to region C. Different LLJs patterns for those regional rainfall result in distinct distributions of convergence and CAPE, which are consistent with the maximum regional rainfall. The results above suggest a close relationship between the WR and two types of LLJs.

Strong synoptic forcing associated with fronts (brown lines) can be seen in both the FR of regions D and E, but in different positions (cf. Figs. 12d,i and 12e,j). It can be seen that such synoptic-scale disturbances are much weaker in the WR of regions A–C. Compared to the FR of region D, the front collocated with the 850-hPa SLLJ to its south moves southeastward

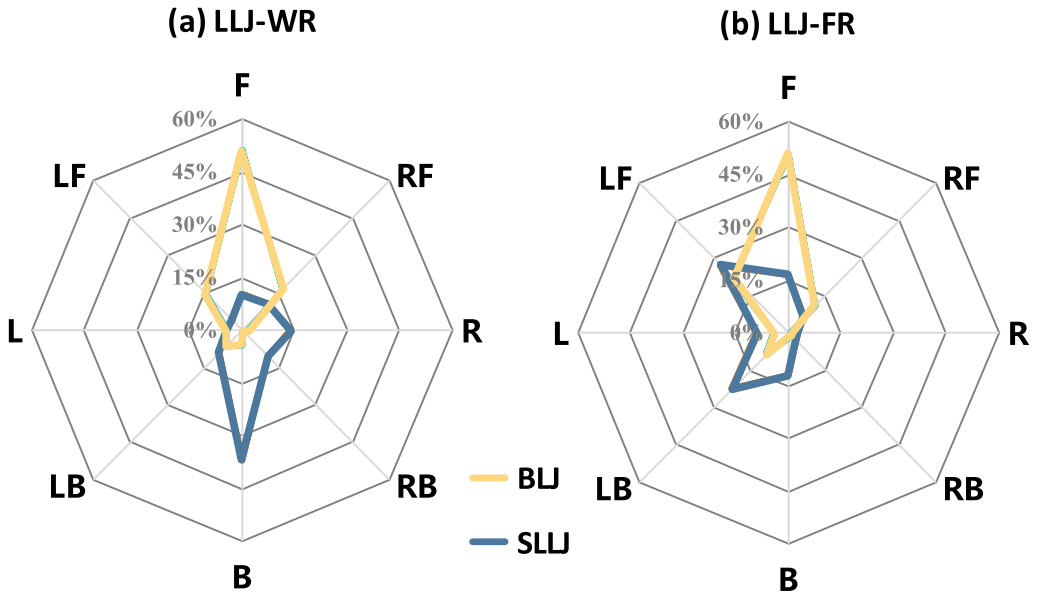

FIG. 13. Occurrence frequencies (%) for the locations of (a) LLJ-WR and (b) LLJ-FR events relative to BLJ (yellow line) and SLLJ (blue line). Letter F indicates that the heavy rainfall event is located in front of the BLJ (SLLJ). The designations RF, R, RB, B, LB, L, and LF are analogous to F, but for different directions of heavy rainfall relative to LLJ: right front, right, right back, back, left back, left, and left front, respectively.

and is located in eastern South China for the FR of region E (cf. Figs. 12e and 12d). A more pronounced southwesterly BLJ occurs in the northern South China Sea at 950 hPa (cf. Figs. 12j and 12i), transporting high CAPE northeastward to the inland region (Fig. 12t). Stronger convergence associated with frontal lifting and higher CAPE are thus shown near rainfall regions (Figs. 12n,o and 12s,t), contributing to more heavy rainfall. To summarize, the locations, intensities, and morphology of the LLJs can greatly affect the convergence location and CAPE transportation and then regulate the distributions of WR, whereas the frontal lifting with the embedded LLJs plays a significant role in FR production.

d. The location of heavy rainfall relative to LLJs

In the present section, the relationships in locations between the two types of heavy rainfall and LLJs (including BLJs and SLLJs) are discussed. Heavy rainfall events are further categorized according to their locations relative to the LLJs. Based on the orientation of the LLJ's axis and the LLJ's core, eight regions are defined as front (F), right front (RF), right (R), right back (RB), back (B), left back (LB), left (L), and left front (LF). If a jet has two or more cores, all the jet cores are taken into account. The statistical results are illustrated by a plot of wind roses, where each direction represents the location of heavy rainfall relative to the LLJs (e.g., letter F means that heavy rainfall occurs in front of the LLJs). Large differences exist in the relative locations between the LLJ-WR and LLJ-FR events. A majority of WR events occur in the front of BLJ (51%) and the rear of SLLJ (37%), namely at the exit region of BLJ and the entrance region of SLLJ (Fig. 13a). A double-LLJ pattern has been reported by Du and Chen (2019a), which provides mesoscale lifting for the coastal WR. By contrast, FR is more frequent along the left side of the SLLJ axis (59%) as well as at the terminus of BLJ (51%; Fig. 13b).

Figure 14 further illustrates the location of heavy rainfall events accompanied by LLJs. WR in South China occurs more frequently in coastal areas than in inland areas (Fig. 14a). Two BLJ cores over Beibu Gulf and the northern South China Sea are accompanied by two corresponding SLLJ cores over southeastern Guangxi and northeastern Guangdong. Therefore, WR tends to occur at the exit region of BLJ as well as the entrance region of SLLJ. The coupling of oceanic BLJ and inland SLLJ provides low-level convergence and middle-level divergence in the coastal areas (Du and Chen 2019a). However, FR often occurs in inland areas (Fig. 14b). The location of BLJ in the FR resembles that of the WR, while the SLLJ has more westerly wind components in the FR. FR often occurs along the left side of the SLLJ axis where positive vorticity contributes to the growth of convection. The elevated SLLJ can also bring more water vapor to the inland rainfall (Du and Chen 2019b). In contrast, BLJ is more conducive to the moist and warm flow transportation to the coastal rainfall regions. The results above provide a general estimate for the location of heavy rainfall relative to the different types of LLJs.

5. Summary and discussion

Relations between two types of heavy rainfall and LLJs in South China are examined during the presummer rainy season, using 22-yr (1998–2019) high temporal-spatial-resolution ERA5 reanalysis data and TRMM rainfall data. With the combination of objective and subjective methods, the identified heavy rainfall episodes are classified into two types: warm sector heavy rainfall (WR) and frontal heavy rainfall (FR). The two types of heavy rainfall show significant differences in

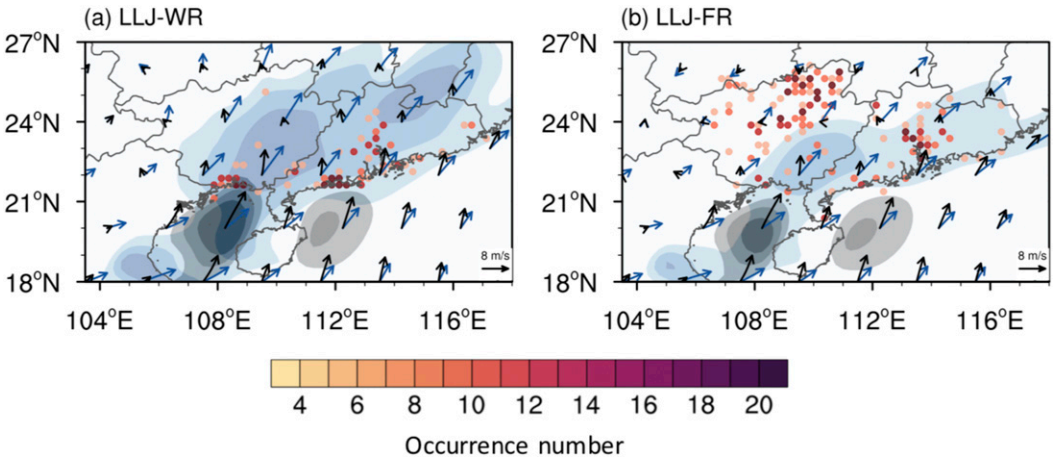

FIG. 14. The colored dots represent various occurrence numbers of (a) LLJ-WR and (b) LLJ-FR events (counted based on the location of maximum heavy rainfall on an event basis). The gray shadings (m s^{-1}) represent composite winds at 950 hPa (≥9 m s^{-1} with an interval of 1 m s^{-1}) and the blue shadings (m s^{-1}) represent composite winds at 850 hPa (≥8 m s^{-1} with an interval of 1 m s^{-1}) during (a) LLJ-WR and (b) LLJ-FR events. The black (blue) vectors denote composite winds at 950 (850) hPa.

spatiotemporal characteristics. WR is mainly concentrated in the coastal areas during the early morning hours, whereas FR mostly occurs over the inland regions with varying rainfall diurnal cycles at different locations due to distinct diurnal forcings. Under relatively weak synoptic forcing, the early morning peak of WR is primarily attributed to the low-level convergence of nocturnal accelerated BLJ and land breeze.

Both WR and FR are found to occur preferentially when LLJs exist. It is found that 76% (62%) of the WR (FR) episodes are related to LLJs. Specifically, the spatial distribution and intensity of WR (FR) are primarily determined by the LLJ periods rather than the non-LLJ periods. During the WR events accompanied by LLJs (LLJ-WR events), there are wide SLLJs at 850 hPa over southeastern Guangxi and northeastern Guangdong and two 950-hPa BLJ cores over Beibu Gulf and the northern South China Sea. Such configuration of the LLJs induces strong coastal convergence and increased convective energy. Comparatively, during the WR events in the absence of LLJs (non-LLJ-WR events), low-level winds are much weaker and other favorable environmental conditions for convection are absent. In addition to LLJs, strong synoptic forcing associated with a front is present during the LLJ-FR events. In contrast, northerly wind perturbations are dominant during the non-LLJ-FR events in the absence of a well-defined front.

Heavy rainfall at different locations is greatly affected by the location, morphology, and strength of the two types of LLJs and associated environmental conditions. The coupling of the BLJ and SLLJ provides mesoscale lifting for WR as well as results in strong moisture transportation but varies regionally. During the WR events of Yangjiang (region B), the upstream BLJ and downstream SLLJ tend to have larger intensity than those of Fangchenggang (region A). In the WR of Shanwei (region C), both BLJ and SLLJ occur farther east and tend to be stronger with more westerly wind components, which is conducive to stronger moisture transportation to region C. Such discrepancies in LLJ structures lead to the position coincidence of coastal convergence and rainfall centers in different regions. Frontal lifting associated with SLLJ embedded in its south occurs farther southeast in the FR of central Guangdong (region E) than that of northern Guangxi (region D), which greatly affects the convergence location and thus the rainfall distribution.

The specific relationships in occurrence frequencies and locations of the two types of heavy rainfall and LLJs are further explored. BLJs are related to both types of heavy rainfall, particularly for WR. On the other hand, SLLJs show a closer relationship with FR. In terms of their relative locations, WR mostly occurs at the exit region of BLJs as well as the entrance region of SLLJs, while FR is often located at the exit of BLJs and along the left side of the SLLJ axis.

The present study clarifies the statistical relationships between the two types of heavy rainfall and LLJs. The conclusions can also be further extended and enhanced with the use of dense observations and high-resolution WRF simulations in order to examine the finer structure of heavy rainfall and LLJs. In the future, the effects of two types of LLJs interacting with other factors (e.g., terrain, cold pool, land–sea contrast, etc.) on heavy rainfall need to be explored in statistics.

Acknowledgments. This study was supported by the National Key Research and Development Program of China (Grant 2018YFC1507402), the National Natural Science Foundation of China (Grants 41875055, 42122033, 4181164027, and 42075006), Guangzhou Science and Technology Plan Projects (202002030346 and 202002030196), the Fundamental Research Funds for the Central Universities (19lgzd08), and the Young Elite Scientists Sponsorship Program by CAST (2018QNRC001).

Data availability statement. The Tropical Rainfall Measuring Mission 3B42V7 data can be downloaded online (https://doi.org/10.5067/TRMM/TMPA/3H/7), and the ERA5 reanalysis data are available online (https://cds.climate.copernicus.eu/#!/search?text=ERA5&type=dataset).

REFERENCES

Beebe, R. G., and F. C. Bates, 1955: A mechanism for assisting in the release of convective instability. *Mon. Wea. Rev.*, **83**, 1–10, https://doi.org/10.1175/1520-0493(1955)083<0001:AMFAIT>2.0.CO;2.

Blackadar, A. K., 1957: Boundary layer wind maxima and their significance for the growth of nocturnal inversions. *Bull. Amer. Meteor. Soc.*, **38**, 283–290, https://doi.org/10.1175/1520-0477-38.5.283.

Chen, G. T.-J., and C.-C. Yu, 1988: Study of low-level jet and extremely heavy rainfall over northern Taiwan in the mei-yu season. *Mon. Wea. Rev.*, **116**, 884–891, https://doi.org/10.1175/1520-0493(1988)116<0884:SOLLJA>2.0.CO;2.

Chen, G. X., W. Sha, T. Iwasaki, and Z. Wen, 2017: Diurnal cycle of a heavy rainfall corridor over East Asia. *Mon. Wea. Rev.*, **145**, 3365–3389, https://doi.org/10.1175/MWR-D-16-0423.1.

——, R. Lan, W. Zeng, H. Pan, and W. Li, 2018: Diurnal variations of rainfall in surface and satellite observations at the monsoon coast (South China). *J. Climate*, **31**, 1703–1724, https://doi.org/10.1175/JCLI-D-17-0373.1.

Chen, X., F. Zhang, and K. Zhao, 2017: Influence of monsoonal wind speed and moisture content on intensity and diurnal variations of the mei-yu season coastal rainfall over South China. *J. Atmos. Sci.*, **74**, 2835–2856, https://doi.org/10.1175/JAS-D-17-0081.1.

Ding, Y. H., 1994: *Monsoons over China*. Kluwer Academic Publishers, 419 pp.

Du, Y., and G. Chen, 2018: Heavy rainfall associated with double low-level jets over southern China. Part I: Ensemble-based analysis. *Mon. Wea. Rev.*, **146**, 3827–3844, https://doi.org/10.1175/MWR-D-18-0101.1.

——, and ——, 2019a: Heavy rainfall associated with double low-level jets over southern China. Part II: Convection initiation. *Mon. Wea. Rev.*, **147**, 543–565, https://doi.org/10.1175/MWR-D-18-0102.1.

——, and ——, 2019b: Climatology of low-level jets and their impact on rainfall over southern China during the early-summer rainy season. *J. Climate*, **32**, 8813–8833, https://doi.org/10.1175/JCLI-D-19-0306.1.

——, Q. Zhang, Y. Ying, and Y. Yang, 2012: Characteristics of low-level jets in Shanghai during the 2008–2009 warm seasons as inferred from wind profiler radar data. *J. Meteor. Soc. Japan*, **90**, 891–903, https://doi.org/10.2151/jmsj.2012-603.

——, G. Chen, Y. Chen, Y. Zhao, and X. Wang, 2014: Numerical simulations of spatial distributions and diurnal variations of low-level jets in China during early summer. *J. Climate*, **27**, 5747–5767, https://doi.org/10.1175/JCLI-D-13-00571.1.

——, ——, B. Han, C. Mai, L. Bai, and M. Li, 2020a: Convection initiation and growth at the coast of South China. Part I: Effect of the marine boundary layer jet. *Mon. Wea. Rev.*, **148**, 3847–3869, https://doi.org/10.1175/MWR-D-20-0089.1.

——, ——, ——, L. Bai, and M. Li, 2020b: Convection initiation and growth at the coast of South China. Part II: Effects of the terrain, coastline, and cold pools. *Mon. Wea. Rev.*, **148**, 3871–3892, https://doi.org/10.1175/MWR-D-20-0090.1.

Higgins, R. W., Y. Yao, E. S. Yarosh, J. E. Janowiak, and K. C. Mo, 1997: Influence of the great plains low-level jet on summertime precipitation and moisture transport over the central United States. *J. Climate*, **10**, 481–507, https://doi.org/10.1175/1520-0442(1997)010<0481:IOTGPL>2.0.CO;2.

Hodges, D., and Z. Pu, 2018: Characteristics and variations of low-level jets in the contrasting warm season precipitation extremes of 2006 and 2007 over the Southern Great Plains. *Theor. Appl. Climatol.*, **136**, 753–771, https://doi.org/10.1007/s00704-018-2492-7.

Holton, J. R., 1967: The diurnal boundary layer wind oscillation above sloping terrain. *Tellus*, **19**, 200–205, https://doi.org/10.3402/tellusa.v19i2.9766.

Huang, L., and Y. Luo, 2017: Evaluation of quantitative precipitation forecasts by TIGGE ensembles for South China during the presummer rainy season. *J. Geophys. Res.*, **122**, 8494–8516, https://doi.org/10.1002/2017JD026512.

Huang, S. S., 1986: *Heavy Rainfall over Southern China in the Pre-Summer Rainy Season* (in Chinese). Guangdong Science and Technology Press, 244 pp.

Huffman, G. J., and Coauthors, 2007: The TRMM Multisatellite Precipitation Analysis (TMPA): Quasi-global, multiyear, combined-sensor precipitation estimates at fine scales. *J. Hydrometeor.*, **8**, 38–55, https://doi.org/10.1175/JHM560.1.

Jiang, Z., D. Zhang, R. Xia, and T. Qian, 2017: Diurnal variations of presummer rainfall over southern China. *J. Climate*, **30**, 755–773, https://doi.org/10.1175/JCLI-D-15-0666.1.

Li, Z., Y. Luo, Y. Du, and J. C. L. Chan, 2020: Statistical characteristics of pre-summer rainfall over South China and associated synoptic conditions. *J. Meteor. Soc. Japan*, **98**, 213–233, https://doi.org/10.2151/jmsj.2020-012.

Liu, H., M. He, B. Wang, and Q. Zhang, 2014: Advances in low-level jet research and future prospects. *Acta Meteor. Sin.*, **28**, 57–75, https://doi.org/10.1007/s13351-014-3166-8.

Liu, R., J. Sun, and B. Chen, 2019: Selection and classification of warm-sector heavy rainfall events over South China. *Chin. J. Atmos. Sci.*, **43**, 119–130, https://doi.org/10.3878/j.issn.1006-9895.1803.17245.

Luo, Y., and Coauthors, 2017: The Southern China Monsoon Rainfall Experiment (SCMREX). *Bull. Amer. Meteor. Soc.*, **98**, 999–1013, https://doi.org/10.1175/BAMS-D-15-00235.1.

Shen, Y., A. Xiong, Y. Wang, and P. Xie, 2010: Performance of high-resolution satellite precipitation products over China. *J. Geophys. Res.*, **115**, D02114, https://doi.org/10.1029/2009JD012097.

Sun, J., Y. Zhang, R. Liu, S. Fu, and F. Tian, 2019: A review of research on warm-sector heavy rainfall in China. *Adv. Atmos. Sci.*, **36**, 1299–1307, https://doi.org/10.1007/s00376-019-9021-1.

Tao, S., and L. Chen, 1987: A review of recent research on the East Asian summer monsoon in China. *Monsoon Meteorology*, C.-P. Chang and T. N. Krishnamurti, Eds., Oxford University, 60–92.

Walters, C. K., and J. A. Winkler, 2001: Airflow configurations of warm season southerly low-level wind maxima in the Great Plains. Part I: Spatial and temporal characteristics and relationship to convection. *Wea. Forecasting*, **16**, 513–530, https://doi.org/10.1175/1520-0434(2001)016<0513:ACOWSS>2.0.CO;2.

Wu, N., X. Ding, Z. Wen, G. Chen, Z. Meng, L. Lin, and J. Min, 2020: Contrasting frontal and warm-sector heavy rainfalls over South China during the early-summer rainy season. *Atmos. Res.*, **235**, 104693, https://doi.org/10.1016/j.atmosres.2019.104693.

Xia, R., and S. Zhao, 2009: Diagnosis and modeling of meso-β-scale systems of heavy rainfall in warm sector ahead of front in South China (middle part of Guangdong Province) in June 2005. *Chin. J. Atmos. Sci.*, **33**, 468–488.

——, ——, and J. Sun, 2006: A study of circumstances of meso-β-scale systems of strong heavy rainfall in warm sector ahead of fronts in South China. *Chin. J. Atmos. Sci.*, **30**, 988–1008.

Xie, Y., 1956: A preliminary survey of certain rain-bearing systems over China in spring and summer. *Acta Meteor. Sin.*, **1**, 1–23.

Xue, M., X. Luo, K. Zhu, Z. Sun, and J. Fei, 2018: The controlling role of boundary layer inertial oscillations in Meiyu frontal precipitation and its diurnal cycles over China. *J. Geophys. Res.*, **123**, 5090–5115, https://doi.org/10.1029/2018JD028368.

Zhang, M., and Z. Meng, 2019: Warm-sector heavy rainfall in southern China and its WRF simulation evaluation: A low-level-jet perspective. *Mon. Wea. Rev.*, **147**, 4461–4480, https://doi.org/10.1175/MWR-D-19-0110.1.

Zhang, W., and J. Zhou, 2003: The role of inertial stability in heavy rain accompanied by upper and low level jets. *J. Nanjing Inst. Meteor.*, **26**, 474–480.

Zhang, X., and Y. Ni, 2009: A comparative study of a frontal and a non-frontal convective systems. *Acta Meteor. Sin.*, **67**, 108–121.

Zhang, Y., M. Xue, K. Zhu, and B. Zhou, 2019: What is the main cause of diurnal variation and nocturnal peak of summer precipitation in Sichuan basin, China? The key role of boundary layer low-level jet inertial oscillations. *J. Geophys. Res.*, **124**, 2643–2664, https://doi.org/10.1029/2018JD029834.